University Library



A gateway to Melbourne's research publications

Minerva Access is the Institutional Repository of The University of Melbourne

Author/s:
McCoey, JM;Matsuoka, M;de Gille, RW;Hall, LT;Shaw, JA;Tetienne, J-P;Kisailus, D;Hollenberg, LCL;Simpson, DA

Title:
Quantum Magnetic Imaging of Iron Biomineralization in Teeth of the Chiton Acanthopleura hirtosa

Date:
2020-03-13

Citation:
McCoey, J. M., Matsuoka, M., de Gille, R. W., Hall, L. T., Shaw, J. A., Tetienne, J. -P., Kisailus, D., Hollenberg, L. C. L. & Simpson, D. A. (2020). Quantum Magnetic Imaging of Iron Biomineralization in Teeth of the Chiton Acanthopleura hirtosa. Small Methods, 4 (3), https://doi.org/10.1002/smtd.201900754.

Persistent Link:
https://hdl.handle.net/11343/271005

Check for updates

Quantum Magnetic Imaging of Iron Biomineralization in Teeth of the Chiton *Acanthopleura hirtosa*

Julia M. McCoey, Mirai Matsuoka, Robert W. de Gille, Liam T. Hall, Jeremy A. Shaw, Jean-Philippe Tetienne, David Kisailus, Lloyd C. L. Hollenberg, and David A. Simpson**

J. M. McCoey, M. Matsuoka, R. W. de Gille, Dr. L. T. Hall, Dr. J.-P. Tetienne, Prof. L. C. L. Hollenberg, Dr. D. A. Simpson

School of Physics, The University of Melbourne, Parkville, 3010, VIC, Australia

Dr. J. A. Shaw

Center for Microscopy, Characterisation and Analysis, University of Western Australia, Perth, 6009, WA, Australia

Prof. D. Kisailus

Department of Chemical and Environmental Engineering, Bourns Hall B357, Riverside, CA 92521, USA

E-mail: simd@unimelb.edu.au & jmccoey@unimelb.edu.au

Keywords: biomineralization, diamond, magnetic imaging, chiton, nitrogen-vacancy

Author Manuscript

This is the author manuscript accepted for publication and has undergone full peer review but has not been through the copyediting, typesetting, pagination and proofreading process, which may lead to differences between this version and the Version of Record. Please cite this article as doi: 10.1002/smtd.201900754.

This article is protected by copyright. All rights reserved.

Iron is critical for life. Nature capitalises on the physical attributes of iron biominerals for functional, structural and sensory applications. Iron biomineralization is well exemplified by the magnetite-bearing radula of chitons, the hardest known biomineral of any animal. Although magnetism is an integral property of iron biominerals, limited information exists on the magnetic state, structure and orientation of these nanoscale materials during mineralization. The advent of quantum based magnetic microscopy provides a new avenue to probe these biological systems directly, providing detailed magnetic information of the iron oxide structures. Here we apply two complementary quantum magnetic microscopy methods, based on nitrogen-vacancy centers in diamond, to spatially map the mineral phases ferrihydrite and magnetite in the developing teeth of the chiton *Acanthopleura hirtosa*. The images reveal previously undiscovered long-range magnetic order, established at the onset of magnetite mineralization. This is in contrast to electron microscopy studies that show no strong common crystallographic orientation. The implications of these results are important, not just for the insights gained in biomineralization of the target organism, but also for the study of a broad range of iron minerals in the physical and biological sciences.

Author Manuscript

1. Introduction

Chitons represent an ideal model system to study iron biomineralization. Anatomically, they possess eight hard dorsal plates and a soft body, with a ventrally-facing mouth (**Figure** 1a). Chitons require structurally hard teeth because of their feeding habits. They are omnivorous grazers, rasping food from rocky substrates with their radula, a tongue-like organ with rows of curved teeth. The fully developed teeth possess material properties equivalent to the hardest structural ceramics.[1] These abrasion- and load-resistant properties are due to the biogenic magnetite capping of the tooth cusp.[2] In chitons, a single radula contains many rows of teeth, with each tooth row progressing in discrete stages from an unmineralised to a fully mineralised state.[3]

The major iron minerals that compose the structure of mature teeth in the Australian chiton *Acanthopleura hirtosa*[4] are magnetite, goethite, and calcium apatite (Figure 1b). While the mechanical properties and mineral composition of mature chiton teeth have been studied extensively in multiple species[1, 5-7], little is known about the growth and transformation of the iron biomineral phases and their organization at the early stages of mineralization.

This article is protected by copyright. All rights reserved.

To investigate the magnetic organization of the iron biominerals at the early stages of development, a quantum-based magnetic imaging approach[8, 9] is employed that combines high-resolution spatial imaging with quantitative mapping of static and fluctuating magnetic fields to study *in-situ* mineral phases. Our diamond-based magnetic microscope provides subcellular magnetic profiling while distinguishing the magnetic signals from magnetite and ferrihydrite.

2. Results

2.1. Magnetite imaging via static magnetic field

To image the spatial distribution of iron-containing minerals, we designed and constructed a quantum-based magnetic microscope, which exploits the magnetic sensitivity of atomic defects in diamond.[10] Our system consists of an inverted optical wide-field microscope with a diamond sensing chip containing a 2D array of negatively charged nitrogen-vacancy (NV) centers engineered approximately 6-8 nm beneath the diamond surface (Figure 1c), see methods. The NV center in diamond is an atomic point defect consisting of a substitutional nitrogen atom and an adjacent vacancy aligned along one of four possible <111> crystallographic orientations. The NV center can exist in the neutral or negatively charged state. A simplified schematic of the electronic structure of the negatively charged NV center, referred to as NV from hereon is shown in Figure 1d. The NV center possesses two unpaired electrons resulting in a spin 1 system with a diamond crystal field splitting of 2.87 GHz separating the $|0\rangle \rightarrow |\pm1\rangle$ ground spin states. The $|\pm1\rangle$ ground spin states Zeeman split in the presence of a local magnetic field by $\Delta E = 2\gamma_0 B_{NV}$, where γ_0 is the NV

This article is protected by copyright. All rights reserved.

Author Manuscript

gyromagnetic ratio = 2.8 MHz/G. The NV centers are conveniently spin polarised at room temperature into the m_s = 0 ground spin state using green (532 nm) laser light.[10] The spin-dependent NV fluorescence (637-800 nm) can be imaged onto a sCMOS camera, allowing optically detected magnetic resonance (ODMR) of the ground state energy levels to be performed at each imaging pixel of the sensing array.[11, 12] A separate imaging protocol based on the measurement of the spin relaxation time (T_1) of the NV spins is used for sensing fluctuating magnetic fields.[13, 14] In this protocol, the NV spins are polarised using pulsed green excitation and then left to evolve in the dark for a variable time, τ, before optical spin readout. Both quantum sensing protocols are used to image the magnetic properties of chiton teeth before, during and post the onset of mineralization: ODMR was used to image the static vector magnetic fields from magnetite (Figure 1e) via the Zeeman splitting of the ground state energy levels, while quantum relaxation microscopy was used to image the magnetic fluctuations from superparamagnetic ferrihydrite (Figure 1f) by monitoring changes in the NV spin lattice relaxation time. Imaging may be performed consecutively without any adjustment of the sample or microscope setup.

Acanthopleura hirtosa radulae were set in resin and sectioned for imaging as shown in **Figure 2**a. Correctly orienting the section through the tooth is crucial to achieve an accurate interpretation of the tooth structure. Critically, this is the first study to use X-ray tomography during the sample preparation workflow, facilitating the targeted collection of tooth sections from known orientations. This provides absolute certainty when interpreting ODMR data with respect to the tooth's microstructure across various length scales and places the observed information in precise context with the tooth's functional properties. Because the radula provides a series of progressive snapshots

Author Manuscript

This article is protected by copyright. All rights reserved.

of tooth development, we sectioned multiple teeth from the same radula. Teeth are numbered from less mineralised to more mineralised, with the first tooth that displays orange colouration being tooth zero. Sections were cut to show the tooth preceding mineralization (tooth -1), at the onset of mineralization (tooth 0), and more advanced stages of mineralization where phase transformations to magnetite have occurred (teeth 3 and 4).

The microtomed tooth sections were mounted on the diamonds for imaging, see methods. Figure 2b and c show the microtomed sections of teeth 3 and 4 on the diamond. At room temperature, magnetite particles are ferrimagnetic and therefore present a stable static magnetic field that can be imaged via ODMR (Figure 2d). The magnetic field strength from the magnetite nanoparticles can be measured via the Zeeman splitting of the NV energy levels obtained from the ODMR spectrum at each pixel, resulting in a 2D magnetic field map. A weak uniform background field of 30 G was applied to the sample to obtain the magnetic field map in Figure 2d. The background field was sufficient to separate the four NV orientations, but an order of magnitude below the magnetic coercivity of the magnetite nanoparticles, $H_c \sim$ 800-900 G for particles > 30 nm.[15] The background magnetic field contribution is removed by subtracting the average magnetic field from a 20 μm^2 region off the tooth, see methods for more information. All teeth were imaged in this mode, see supplementary information. No static magnetic signals were detected from tooth -1, indicating no ferrimagnetic magnetite nanoparticles, consistent with this stage of tooth development in *A. hirtosa.*[16] Magnetic signals corresponding to the posterior surface of tooth 0 were resolved, see supplementary information, and the strength of the static magnetic signal increases for both tooth 3

Author Manuscript

This article is protected by copyright. All rights reserved.

and 4 as shown in Figure 2e and f, recall that these magnetic images represent the magnitude of the magnetic field along a given NV axis.

Author Manuscript

2.2. Vector magnetic imaging of magnetite

To determine the magnitude and direction of the magnetite's magnetization, we measure the full magnetic field vector at each imaging pixel. To implement this capability, we applied a weak and uniform background field of 30 G sequentially along each NV axis using a three-axis Helmholtz coil. This permits measurement of the magnetic field projection along each of the four NV crystallographic axes. We used the magnetic field projections along three NV axes to reconstruct the x, y and z projections (**Figure 3**a and b) of the vector field.

The vector magnetic field maps show long-range magnetic order extending over the entire tooth section, with a broadly uniform magnetite magnetization, oriented perpendicular to the plane of the section (Figure 3c). This long-range magnetic order is surprising, because at this stage of mineralization, the magnetite particles are small and disconnected, without any orientational organization evident in their individual visible structure alone, see supplementary information. Therefore, the long-range magnetic ordering indicates either that crystals were actively aligned by the underlying organic matrix, or that the particles were magnetically coupled as they transitioned into a ferrimagnetic state. Disturbances in the magnetic field due to fractures in the tooth from sectioning are also clearly resolvable (Figure 3d and e). A simplified magnetic model of tooth architecture supports the out of plane magnetization finding, see supplementary information. Full

This article is protected by copyright. All rights reserved.

vector maps of tooth 4 are also provided in the supplementary information with both teeth exhibiting similar magnetic profiles.

Previous work has identified anisotropy of magnetization in the mature tricuspid teeth of *Acanthochiton rubrolinestus*,[17, 18] where the length and width of the teeth are more easily magnetised than the thickness.[19] Our vector magnetic microscopy images provide the first evidence of magnetic organization at the microscale level in the chiton radula. We demonstrate that for *A. hirtosa,* in the early stages of tooth development, the magnetite nanoparticles are magnetised perpendicular to the plane of the section, i.e. across the tooth width.

Biomineralization has, in multiple instances, been shown to occur via non-classical routes, including mesocrystalline intermediate stages and crystallization by particle attachment.[20] The possibility of a mesocrystalline formation mechanism was first raised for chiton biomineralization upon the discovery of grain substructure in mature *A. hirtosa* teeth.[21] Our results support the presence of a magnetic mesocrystalline phase in the tooth cusp, preceding the ordered rods of magnetite in a mature tooth,[22] as overall order is seen in the magnetic vector maps on a scale larger than any individual faceted crystal. It has been proposed that the collective magnetic field produced by the cumulative fields of aligned nanocrystals in a mesocrystalline colloid could assist the formation of a magnetic solid.[23] It is conceivable, therefore, that the magnetic field produced by the alignment of the early magnetite nanoparticles may assist in the synthesis of the magnetite rods.

Author Manuscript

This article is protected by copyright. All rights reserved.

Author Manuscript

2.3. Magnetic microscopy of ferrihydrite

Prior to magnetite crystallization, iron is present but not in a ferrimagnetic form. The first iron mineral to be deposited within the tooth is 6-line ferrihydrite, the predominant form of iron within ferritin.[24, 25] Ferrihydrite is a ferric oxyhydroxide and superparamagnetic at room temperature.[26] Ferrihydrite particles are less than 10 nm in size,[27] with a superparamagnetic fluctuation spectrum of order 1 GHz, see supplementary information Fig. S4 – S6. This magnetic fluctuation frequency conveniently overlaps with the NV transition energies from the $|0\rangle$ to $|\pm1\rangle$ states at zero magnetic field. By monitoring the spin relaxation rate ($1/T_1$) of the NV centers across the full field of view,[28] see methods, we can detect and map the fluctuating magnetic fields from ferrihydrite directly, in a technique we term quantum relaxation microscopy (QRM).

Using QRM, we find the ferrihydrite concentration increases with development (**Figure 4**a), in agreement with studies across chiton species.[29] In teeth -1 and 0, where little or no magnetite is present, ferrihydrite is detected along the posterior face of the tooth cusp. In the more mature teeth (3 and 4), the bulk of ferrihydrite is on the anterior side of the magnetite, with a thin layer of ferrihydrite coating the outer, posterior side of the magnetite (Figure 4b and c).

As a mineral phase mapping technique, QRM is highly effective. Elemental mapping across whole *A. hirtosa* teeth has not previously been performed with any other technique; however, elemental and

This article is protected by copyright. All rights reserved.

mineral phase locations have been investigated in other species. Energy dispersive spectroscopy and Raman spectroscopy have been used in combination with scanning electron microscopy to locate ferrihydrite and magnetite regions in the immature unicuspid teeth of *Acanthopleura echinata*.[30] Though not an imaging technique, the *A. echinata* results indicate multiple fronts of mineralization, showing parallels with the present study. The QRM images show that by tooth 4, two distinct regions of ferrihydrite border the bulk of the magnetite region. In addition to the ferrihydrite band that appears on the posterior tooth cusp by tooth 4, the interior band extends further in towards the core of the tooth cusp. This contrasts with the ferrihydrite pattern in the tricuspid teeth of *Cryptochiton stelleri* observed via micro X-ray fluorescence (μXRF).[22] These similarities and differences may be related to the mineralization strategy employed; *A. echinata* and *A. hirtosa* form an apatite core while *C. stelleri* has a hydrated iron phosphate core. Because of the variation in these mineralization strategies, it would be worthwhile in future studies to examine multiple species with the high resolution, whole tooth mapping that QRM provides. The iron biominerals within chiton teeth studied here present two distinct magnetic signatures; however, more advanced stages of mineralization will contain new biomineral phases such as goethite and lepidocrocite. Diamond-based electron spin resonance spectroscopy techniques[31, 32] may allow these specific mineral phases to be mapped and imaged in more mature teeth.

3. Conclusion

The application of quantum-based magnetic microscopy to biological systems presents several key advantages when compared to existing magnetic imaging techniques. Widefield magnetic microscopy allows for rapid acquisition and high throughput when compared to scanning probe techniques such as MFM and transmission electron microscopy (TEM). Nitrogen-vacancy centers

Author Manuscript

This article is protected by copyright. All rights reserved.

provide full vector magnetic imaging capability, which is extremely difficult to achieve in MFM or superconducting quantum interference device (SQUID) systems. Furthermore, studies of long-range magnetic order now become possible as the field of view is increased significantly in comparison to existing methods such as TEM. In our current configuration the magnetic imaging resolution is limited by the diffraction limit of light to ~300 nm^2. The lateral resolution is dictated by the magnetic signal fall-off. For static magnetic signals the resolution is governed by the size of the particles contributing to the signal; for magnetite nanoparticles in chiton teeth this equates to the thickness of the microtomed slice 500 -1000 nm. For superparamagnetic imaging, the magnetic signal fall-off is steeper and ultimately limited by the T_1 time of the NV ensembles. For the diamond sensor used in this work, the lateral resolution is approximately 100 nm. It should be noted that the superior spatial resolution and magnetic sensitivity of quantum-based magnetic microscopy is offset by the fact that it is a 2D imaging technique, unlike PET, MRI and CT. There is opportunity to extend the imaging technique to 3D via multiple sectioning at the expense of time. Quantum-based magnetic microscopy does however compliment the vast array of techniques used to study biological samples such as TEM[33], X-ray magnetic circular dichroism[34], XRF[22], positron emission tomography/CT[35] and photoacoustic imaging[36]. Inevitably, a combination of these imaging techniques will be required to elucidate the complex relationship between the magnetic properties, the crystalline structure of iron biominerals and the underlying organic matrix of chiton teeth.

The precise mechanisms governing the attachment of ferrihydrite to the organic matrix and the subsequent phase transformation remain active areas of research. The magnetic images presented in this work reveal previously undiscovered long-range magnetic order at the onset of magnetite

Author Manuscript

This article is protected by copyright. All rights reserved.

mineralization, in contrast to electron microscopy studies that show no strong common crystallographic orientation. A complete picture of mineralization must now consider the development of magnetic order and its possible effects on the nanoscale assembly of magnetite. We anticipate that the magnetic profiling techniques demonstrated in the present study will become valuable tools for probing such interactions in concert with the current suite of high-resolution electron and X-ray microscopy techniques. Given the interest in biomimetic materials, future work may exploit quantum magnetic microscopy for real time imaging of magnetite assembly using synthetic approaches adapted from biological systems. The unique combination of vector magnetic imaging and QRM on a bio-compatible platform opens a pathway toward mineral-specific imaging of a vast range of biological systems.

Author Manuscript

5. Experimental Section

Materials: The diamond imaging sensor used in this work is engineered from electronic grade Type IIa <111> diamond (Element 6). The diamonds were thinned, cut and re-polished to a 1 × 2 × 0.1 mm^3 crystal (DDK, USA). NV defects were engineered via ion implantation of ^{15}N atoms at an energy of 4 keV and dose of 1×10^{13} ions cm^{-2}. Molecular dynamic simulations indicate a NV depth range between 5-10 nm.[37] The implanted sample was annealed at 1000 °C for three hours and acid treated to remove any unwanted surface contamination. The density of NV centers post annealing was 1×10^{11} NV cm^{-2}.

This article is protected by copyright. All rights reserved.

Sample preparation: Fresh specimens of the chiton *A. hirtosa*[4] were collected and dissected as described previously.[38] Care was taken to avoid exposing the samples to any strong magnetic field from collection to measurement. Briefly, radulae were excised and fixed in 2.5% glutaraldehyde, buffered in 0.1 M phosphate at pH 7.2 (osmotic pressure adjusted to 900 mmol·kg^{-1} using sucrose). Radulae were then fixed, dehydrated, and infiltrated in epoxy resin using microwave-assisted chemical fixation (Pelco, Biowave).

To facilitate the collection of histological sections from precise orientations through the teeth, resin blocks were first scanned using X-ray micro-computed tomography (µCT). Scans were conducted at 80kV and 82 µA using a Versa 520 XRM (Zeiss, Pleasanton, USA) running Scout and Scan software (v11.1.5707.17179, Zeiss). A total of 401 projections were collected over 360^{o}, each with a 1 second exposure. 2x binning was used to achieve a suitable signal to noise ratio and 0.4x optical magnification was used to achieve an isotropic voxel resolution of 12.8 µm. Raw data were reconstructed using XMReconstructor software (v11.1.5707.17179, Zeiss) following a standard center shift and beam hardening correction. The standard 0.7 kernel size recon filter setting was also used. Reconstructed data were observed (TXM3D Viewer, Zeiss) to determine the position of the major lateral teeth relative to the resin block and a razor blade was used to then mark the resin at the correct plane of orientation to produce a longitudinal cut through the middle of each tooth.

Author Manuscript

This article is protected by copyright. All rights reserved.

Resin blocks were then trimmed at this orientation using a glass knife on an ultramicrotome (EM UC6, Leica Microsystems). Once the correct position was reached, 1 µm sections were cut with a diamond knife (Histo, Diatome) onto filtered DI water. Sections were transferred using a wooden applicator stick to a drop of ~70 °C filtered DI water (situated in a Petri dish placed on a hotplate). Sections were left to warm for 1-2 mins on the water drop to assist with smoothing the section. Sections were transferred using a wooden applicator stick to a drop of filtered DI water on the imaging slide. An eyelash mounted on a wooden applicator stick was used to position the section onto the diamond chip and a paper wick was then used to remove excess water from the slide; finally, the sample was air dried.

Optical Imaging: Samples were diamond-imaged in wide-field on a modified Nikon inverted microscope (Ti-U). Optical excitation from a 532 nm Verdi laser was focused (f = 300 mm) onto an acousto-optic modulator (Crystal Technologies Model 3520–220) and then expanded and collimated (Thorlabs beam expander GBE05-A) to a beam diameter of 10 mm. The collimated beam was focused using a wide-field lens (f = 300 mm) to the back aperture of the Nikon x60 (1.4 NA) oil immersion objective via a Semrock dichroic mirror (Di02-R561-25 × 36). The beam was first centerd to the objective, then translated until the beam totally internally reflected within the diamond. The NV fluorescence was filtered using two bandpass filters before being imaged using a tube lens (f = 300 mm) onto a sCMOS camera (Neo, Andor). Microwave excitation to drive the NV spin probes was applied via an omega gold resonator (diameter = 0.8 mm) lithographically patterned onto a glass coverslip directly under the diamond imaging chip. The microwave signal from an Agilent microwave generator (N5182A) was switched using a Minicircuits RF switch (ZASWA-2-50DR+). The microwaves

Author Manuscript

This article is protected by copyright. All rights reserved.

were amplified (Amplifier Research 20S1G4) before being sent to the microwave resonator. A Spincore Pulseblaster (ESR-PRO 500 MHz) was used to control the timing sequences of the excitation laser, microwaves and sCMOS camera and the images where obtained and analysed using custom LabVIEW code. The excitation power density used for imaging was 30 W mm^{-2} and all images were taken in an ambient environment at room temperature.

Quantum relaxation microscopy: To implement quantum relaxation microscopy the spin lattice relaxation time (T_1) of the NV centers was determined by optically polarising the NV spins into the m_s = 0 ground state, then allowing the spins to evolve (in the dark) for a time τ, before sampling their spin polarization with an additional optical pulse. Interactions between the NV centers and neighbouring electronic, nuclear and surface spins species cause the NV net magnetization to relax from the m_s = 0 state to a mixture of the three ground triplet states. The e^{-1} time of the decay is the T_1 time of the NV centers. In this work we normalised the T_1 decay with an identical pulse sequence with a single π pulse applied prior to the spin readout. This provides common mode rejection of noise sources from the NV imaging array. The quantum relaxation microscopy image analysis was performed using custom LabVIEW code.

Electromagnet: Magnetic fields were applied with a custom 3D Helmholtz coil to control both the strength and the direction of the magnetic fields. Copper enamelled wires (ECW0.71) were wound 200-time rounds on each cylindrical side of the Helmholtz coil. To reduce temperature increasing caused by the Joule heating of the copper wires, the coil was manufactured from aluminium and a

Author Manuscript

This article is protected by copyright. All rights reserved.

computer water cooling system (EK CoolStream PE 240 Dual Radiator, EK Vardar 120mm Fan F4-120 2200RPM, and EK-XRES 100 SPC-60 MX PWM Pump/Reservoir Combo) was installed, with water running through a path inside the coil. The power supplier (Hameg HMP2030) was used for generating a static magnetic field.

Image analysis: Custom LabVIEW code was written for image analysis. To produce static magnetic field images, NV fluorescence images were binned 4x4, and ODMR spectra across the two peaks corresponding to the aligned NV axis were obtained for each binned pixel of the image stack. The spectra were fitted with single Lorentzian and the magnetic field strength determined from the peak splitting. The background magnetic field was removed by calculating the average of the 20 × 20 μm area outside of the tooth. This value was subtracted across the full field of view. The resulting magnetic field signal at each binned pixel was saved as an image, and a colour scale applied with ImageJ (Fiji distribution, ImageJ 1.51h). To produce the quantum relaxation images, the NV fluorescence images were binned 4x4, and the T_1 decay curves were obtained for each binned pixel of the image stack. The T_1 decay rate ($1/T_1$) was determined at each binned pixel by fitting the data to a stretched exponential of the form $y = A\,exp^{\left(t/T_1\right)^p} + c$, where A is the amplitude of the exponential decay, T_1 is the spin lattice relaxation time, p is the stretched exponential power (p = 1 represents a single exponential decay) and c is the offset. Near surface NV centers are known to exhibit a distribution of T_1 times from the NV ensemble depending on their proximity to the surface and local spin environment. This distribution leads to a non-exponential T_1 decay which is

Author Manuscript

This article is protected by copyright. All rights reserved.

characterised well by a stretched exponential function. The T_1 rate at each pixel binned pixel was saved as an image, and a colour scale applied with ImageJ (Fiji distribution, ImageJ 1.51h).

Author Manuscript

Supporting Information

Supporting Information is available from the Wiley Online Library or from the author.

Acknowledgements

The authors acknowledge Ashley French for assistance in the design and construction of the Helmholtz coil. This work was supported by the Australian Research Council (ARC) through Grants No. FL130100119, DE170100129. J.-P.T. and L. T. Hall acknowledges support from the University of Melbourne through an Early Career Researcher Grants. D.K acknowledges support from the Army Research Office (W911NF-15-1-0306). The authors acknowledge the facilities, and the scientific and technical assistance of Microscopy Australia at the Center for Microscopy, Characterisation & Analysis, The University of Western Australia, a facility funded by the University, State and Commonwealth Governments.

The authors declare no competing financial interest.

Received: ((will be filled in by the editorial staff))
Revised: ((will be filled in by the editorial staff))
Published online: ((will be filled in by the editorial staff))

References

1. Weaver, J. C.; Wang, Q.; Miserez, A.; Tantuccio, A.; Stromberg, R.; Bozhilov, K. N.; Maxwell, P.; Nay, R.; Heier, S. T.; DiMasi, E.; Kisailus, D., *Materials Today* **2010,** *13* (1), 42-52.
2. Lowenstam, H., *Science* **1967,** *156* (3780), 1373-1375.
3. Joester, D.; Brooker, L. R., *Iron Oxides: From Nature to Applications* **2016**.
4. Blainville, H. M., *Manuel de malacologie et de conchyliologie: contenant [etc.]*. **1825**; Vol. 1.

This article is protected by copyright. All rights reserved.

5. Saunders, M.; Kong, C.; Shaw, J. A.; Clode, P. L., *Microscopy and microanalysis : the official journal of Microscopy Society of America, Microbeam Analysis Society, Microscopical Society of Canada* **2011,** *17* (2), 220-5.
6. Wang, C.; Li, Q.; Wang, S.; Qu, S.; Wang, X., *Materials Science and Engineering: C* **2014,** *37*, 1-8.
7. Grunenfelder, L. K.; de Obaldia, E. E.; Wang, Q.; Li, D.; Weden, B.; Salinas, C.; Wuhrer, R.; Zavattieri, P.; Kisailus, D., *Advanced Functional Materials* **2014,** *24* (39), 6093-6104.
8. Steinert, S.; Dolde, F.; Neumann, P.; Aird, A.; Naydenov, B.; Balasubramanian, G.; Jelezko, F.; Wrachtrup, J., *Rev. Sci. Instrum.* **2010,** *81* (4), 043705.
9. Le Sage, D.; Arai, K.; Glenn, D.; DeVience, S.; Pham, L.; Rahn-Lee, L.; Lukin, M.; Yacoby, A.; Komeili, A.; Walsworth, R., *Nature* **2013,** *496* (7446), 486-489.
10. Doherty, M. W.; Manson, N. B.; Delaney, P.; Jelezko, F.; Wrachtrup, J.; Hollenberg, L. C. L., *Physics Reports* **2013,** *528* (1), 1-45.
11. Simpson, D. A.; Tetienne, J.-P.; McCoey, J. M.; Ganesan, K.; Hall, L. T.; Petrou, S.; Scholten, R. E.; Hollenberg, L. C. L., *Sci Rep* **2016,** *6*, 22797.
12. Tetienne, J.-P.; Dontschuk, N.; Broadway, D. A.; Stacey, A.; Simpson, D. A.; Hollenberg, L. C. L., *Science Advances* **2017,** *3* (4), 1602429.
13. Cole, J. H.; Hollenberg, L. C. L., *Nanotechnology* **2009,** *20* (49), 495401.
14. Hall, L. T.; Cole, J. H.; Hill, C. D.; Hollenberg, L. C. L., *Phys. Rev. Lett.* **2009,** *103* (22), 220802.
15. Dar, M. I.; Shivashankar, S. A., *RSC Advances* **2014,** *4* (8), 4105-4113.
16. Kim, K.-S.; Macey, D.; Webb, J.; Mann, S., *Proceedings of the Royal Society of London. B. Biological Sciences* **1989,** *237* (1288), 335-346.
17. Jian-Gao, Z.; Xia, Q.; Wei, L.; Chuan-Lin, L.; Wen-Shan, Z., *Chinese Physics Letters* **2000,** *17* (7), 542.
18. Han, Y.; Liu, C.; Zhou, D.; Li, F.; Wang, Y.; Han, X., *Bioelectromagnetics* **2011,** *32* (3), 226-233.
19. Qian, X.; Zhao, J. g.; Liu, C. l.; Guo, C. h., *Bioelectromagnetics: Journal of the Bioelectromagnetics Society, The Society for Physical Regulation in Biology and Medicine, The European Bioelectromagnetics Association* **2002,** *23* (6), 480-484.
20. Bergström, L.; Sturm, E. V.; Salazar-Alvarez, G.; Cölfen, H., *Accounts of chemical research* **2015,** *48* (5), 1391-1402.
21. Saunders, M.; Kong, C.; Shaw, J. A.; Macey, D. J.; Clode, P. L., *Journal of structural biology* **2009,** *167* (1), 55-61.
22. Wang, Q.; Nemoto, M.; Li, D.; Weaver, J. C.; Weden, B.; Stegemeier, J.; Bozhilov, K. N.; Wood, L. R.; Milliron, G. W.; Kim, C. S.; DiMasi, E.; Kisailus, D., *Advanced Functional Materials* **2013,** *23* (23), 2908-2917.
23. Lu, Y.; Yin, Y.; Xia, Y., *Adv. Mater.* **2001,** *13* (6), 415-420.
24. Pan, Y.; Brown, A.; Brydson, R.; Warley, A.; Li, A.; Powell, J., *Micron* **2006,** *37* (5), 403-411.
25. Cowley, J.; Janney, D. E.; Gerkin, R.; Buseck, P. R., *Journal of structural biology* **2000,** *131* (3), 210-216.

Author Manuscript

This article is protected by copyright. All rights reserved.

26. Guyodo, Y.; Banerjee, S. K.; Penn, R. L.; Burleson, D.; Berquo, T. S.; Seda, T.; Solheid, P., *Physics of the Earth and Planetary Interiors* **2006,** *154* (3-4), 222-233.
27. Janney, D. E.; Cowley, J. M.; Buseck, P. R., *Clays and Clay Minerals* **2000,** *48* (1), 111-119.
28. Steinert, S.; Ziem, F.; Hall, L.; Zappe, A.; Schweikert, M.; Aird, A.; Balasubramanian, G.; Hollenberg, L.; Wrachtrup, J., *Nat. Commun.* **2013,** *4*, 1607.
29. Gordon, L. M.; Román, J. K.; Everly, R. M.; Cohen, M. J.; Wilker, J. J.; Joester, D., *Angewandte Chemie International Edition* **2014,** *53* (43), 11506-11509.
30. Brooker, L.; Lee, A.; Macey, D.; Van Bronswijk, W.; Webb, J., *Marine Biology* **2003,** *142* (3), 447-454.
31. Hall, L. T.; Kehayias, P.; Simpson, D. A.; Jarmola, A.; Stacey, A.; Budker, D.; Hollenberg, L. C. L., *Nature Communications* **2016,** *7*, 10211.
32. Simpson, D. A.; Ryan, R. G.; Hall, L. T.; Panchenko, E.; Drew, S. C.; Petrou, S.; Donnelly, P. S.; Mulvaney, P.; Hollenberg, L. C. L., *Nature Communications* **2017,** *8* (1), 458.
33. Zhou, Z.; Tian, R.; Wang, Z.; Yang, Z.; Liu, Y.; Liu, G.; Wang, R.; Gao, J.; Song, J.; Nie, L., *Nature communications* **2017,** *8*, 15468.
34. Iacocca, E.; Liu, T.-M.; Reid, A.; Fu, Z.; Ruta, S.; Granitzka, P.; Jal, E.; Bonetti, S.; Gray, A.; Graves, C., *Nature communications* **2019,** *10* (1), 1756.
35. Liu, Y.; Lv, X.; Liu, H.; Zhou, Z.; Huang, J.; Lei, S.; Cai, S.; Chen, Z.; Guo, Y.; Chen, Z., *Nanoscale* **2018,** *10* (8), 3631-3638.
36. Liu, Y.; Kang, N.; Lv, J.; Zhou, Z.; Zhao, Q.; Ma, L.; Chen, Z.; Ren, L.; Nie, L., *Adv. Mater.* **2016,** *28* (30), 6411-6419.
37. Lehtinen, O.; Naydenov, B.; Börner, P.; Melentjevic, K.; Müller, C.; McGuinness, L. P.; Pezzagna, S.; Meijer, J.; Kaiser, U.; Jelezko, F., *Phys. Rev. B* **2016,** *93* (3), 035202.
38. Shaw, J. A.; Macey, D. J.; Clode, P. L.; Brooker, L. R.; Webb, R. I.; Stockdale, E. J.; Binks, R. M., *American Malacological Bulletin* **2008,** *25* (1), 35-42.
39. Tetienne, J.-P.; Broadway, D.; Lillie, S.; Dontschuk, N.; Teraji, T.; Hall, L.; Stacey, A.; Simpson, D.; Hollenberg, L., *Sensors* **2018,** *18* (4), 1290.
40. Gossuin, Y.; Gillis, P.; Hocq, A.; Vuong, Q. L.; Roch, A., *Wiley Interdisciplinary Reviews: Nanomedicine and Nanobiotechnology* **2009,** *1* (3), 299-310.

Author Manuscript

This article is protected by copyright. All rights reserved.

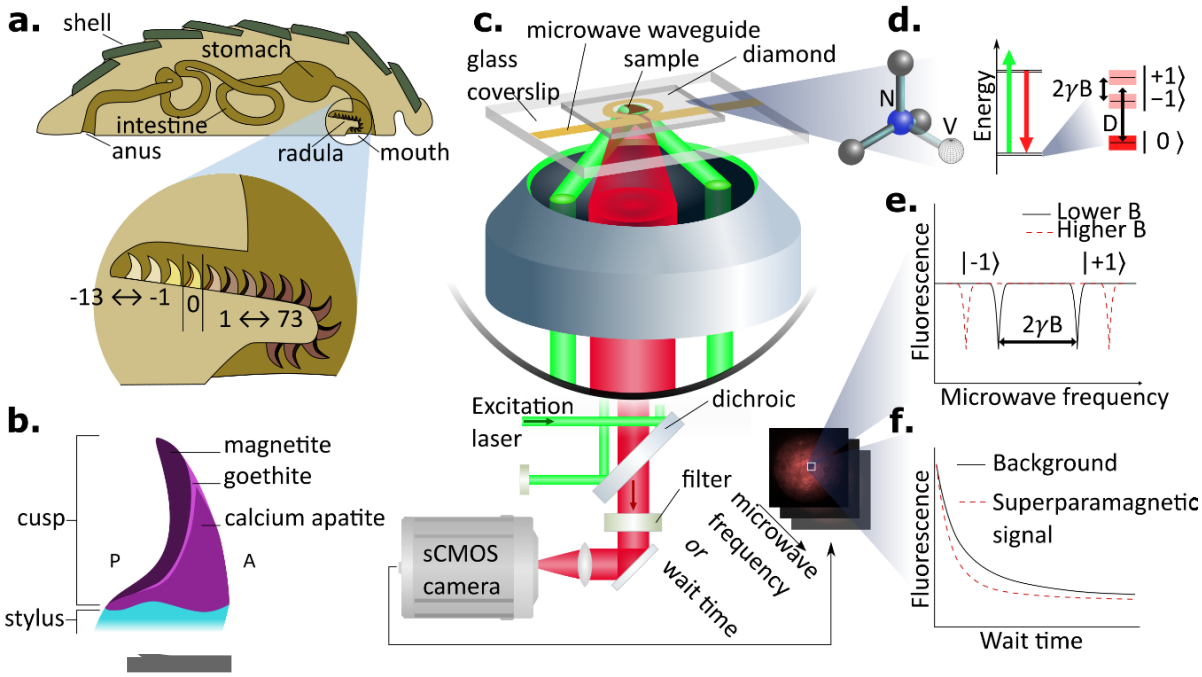


Figure 1. Quantum magnetic microscopy for studying iron-based biomineralization. a, Chiton sagittal section. Enlargement shows the radula – an organ hosting rows of teeth which develop in a conveyor belt-like fashion. The entire tooth development (87 tooth rows in *A. hirtosa*) is seen in one radula. b, The fully mature tooth cusp mineral structure of *A. hirtosa*, median longitudinal cut. c, Optical set-up of quantum magnetic microscope. The diamond sensing chip is excited via total internal reflection and the resulting fluorescence image is captured on an sCMOS camera. d, Schematic of the crystalline structure of the nitrogen vacancy (NV) center in diamond, and relevant energy levels. e, Optically detected magnetic resonance schematic for imaging ferrimagnetic (magnetite) minerals. f, Quantum relaxation microscopy schematic for imaging superparamagnetic (ferrihydrite) minerals.

Author Manuscript

This article is protected by copyright. All rights reserved.

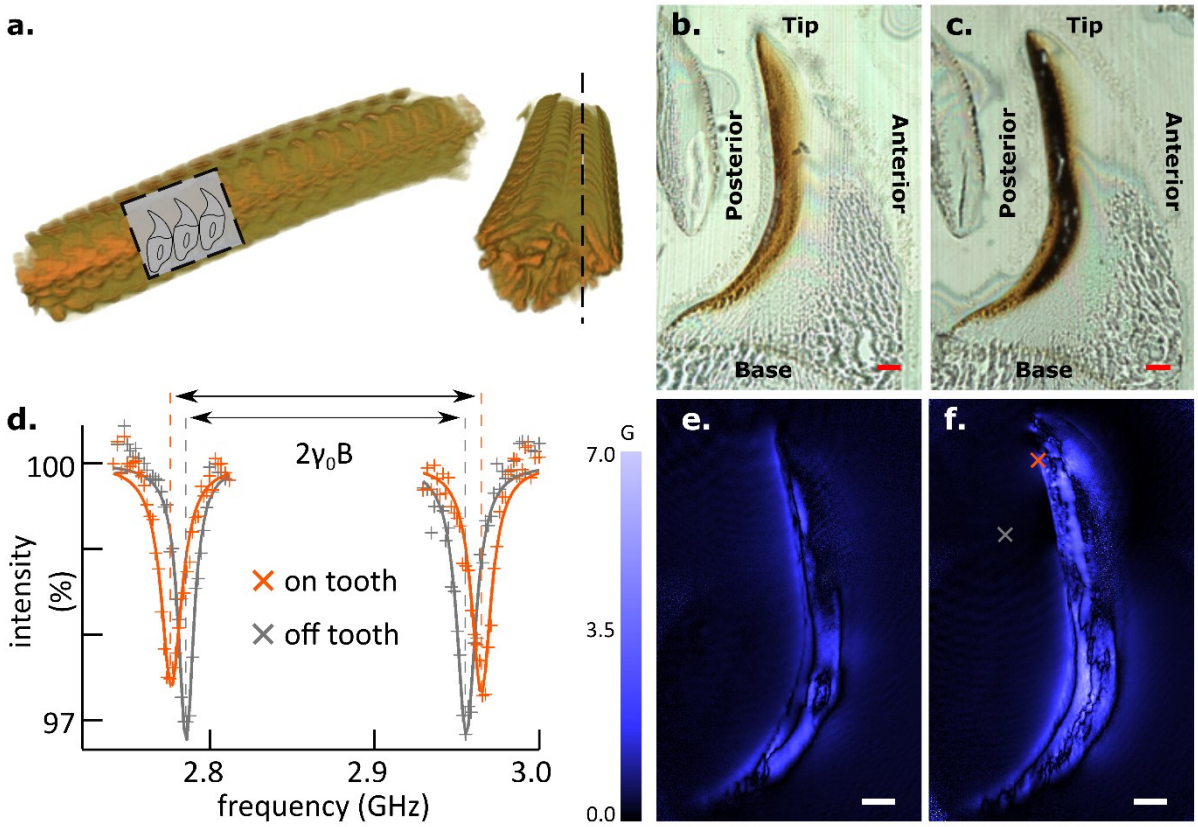


Figure 2. Sample sectioning and magnetic imaging. a, Radula set in resin, and microCT to facilitate longitudinal sectioning, dotted line. One micron thick slices of b, tooth 3, c, tooth 4, were mounted on the diamond sensing chip, red scale bar 20 µm. d, Optically detected magnetic resonance (ODMR) spectra were measured at each imaging pixel across the entire tooth section. The separation of the ODMR transitions is proportional to local magnetic field $\Delta f = 2\gamma_0 B$, where the gyromagnetic ratio of the NV center γ_0 = 2.8 MHz/G. e and f, show the magnitude of the measured magnetic field projection along a single NV axis at 109.5° from the normal for tooth 3 and 4, respectively. Crosses in f correspond to ODMR spectra in d. The white scale bar represents 20 µm.

Author Manuscript

This article is protected by copyright. All rights reserved.

Author Manuscript

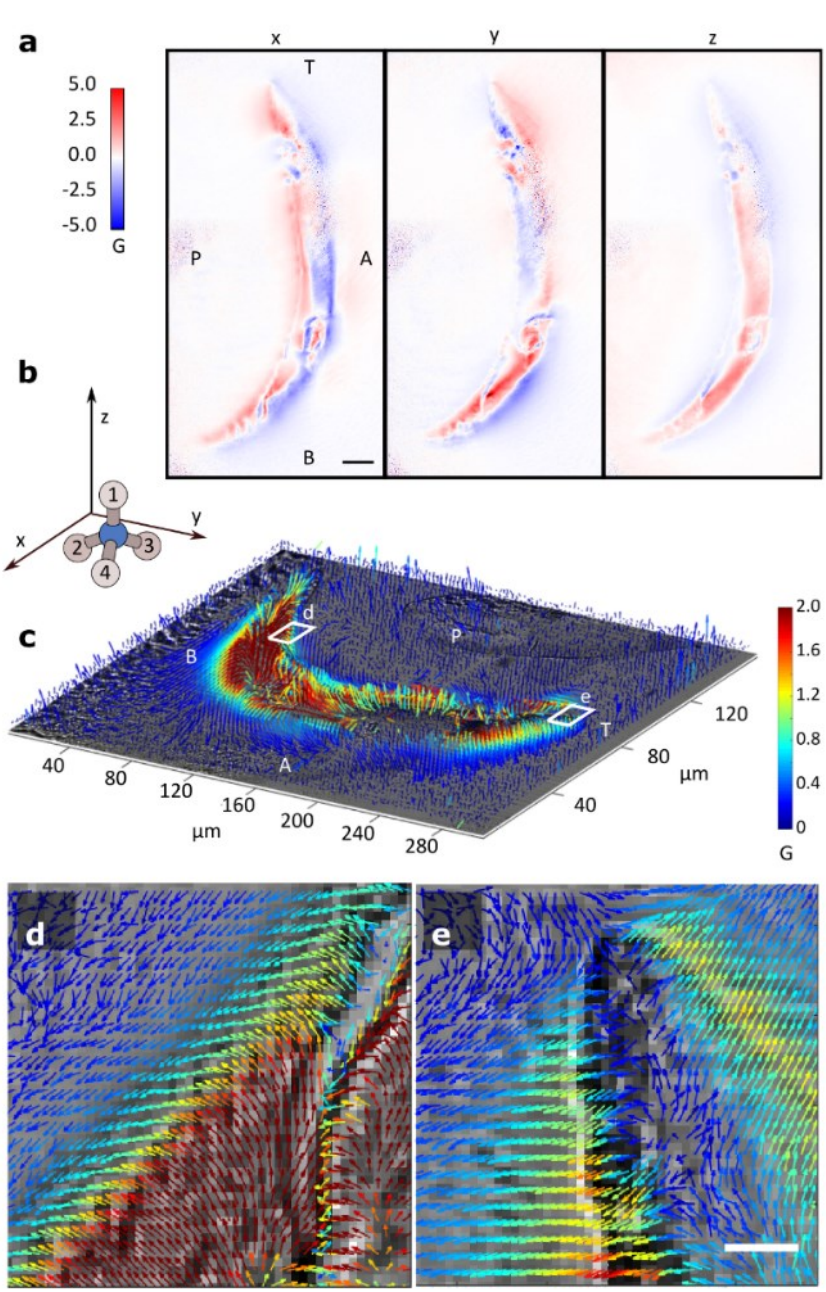


Figure 3. Vector magnetic field imaging of chiton teeth. a, maps of the x, y and z, (out-of-plane) components of the magnetic field, reconstructed from the four NV axes' maps. Letters indicate A anterior, P posterior, T tip, B base. b, Relative orientations of the diamond crystal axes and cartesian axes, as in c. c, Magnetic vector reconstruction of whole tooth cusp section of tooth 3. Colour scale

This article is protected by copyright. All rights reserved.

represents magnitude of the magnetic field and the arrow direction represents magnetic field vector. To aid in visibility of signal from noise, a filter was applied reducing arrow length of noisy vectors. The vector reconstruction is performed by measuring the magnetic field projection along three known crystallographic directions of NV centers in diamond. The vector reconstruction is performed at each imaging pixel with a spatial resolution dictated by the diffraction limit of the microscope, 300 nm. d, e, High resolution vector magnetic field maps of the x and y field components reveal long-range ordering along the tooth cusp, from base to tip, scale bar 2µm.

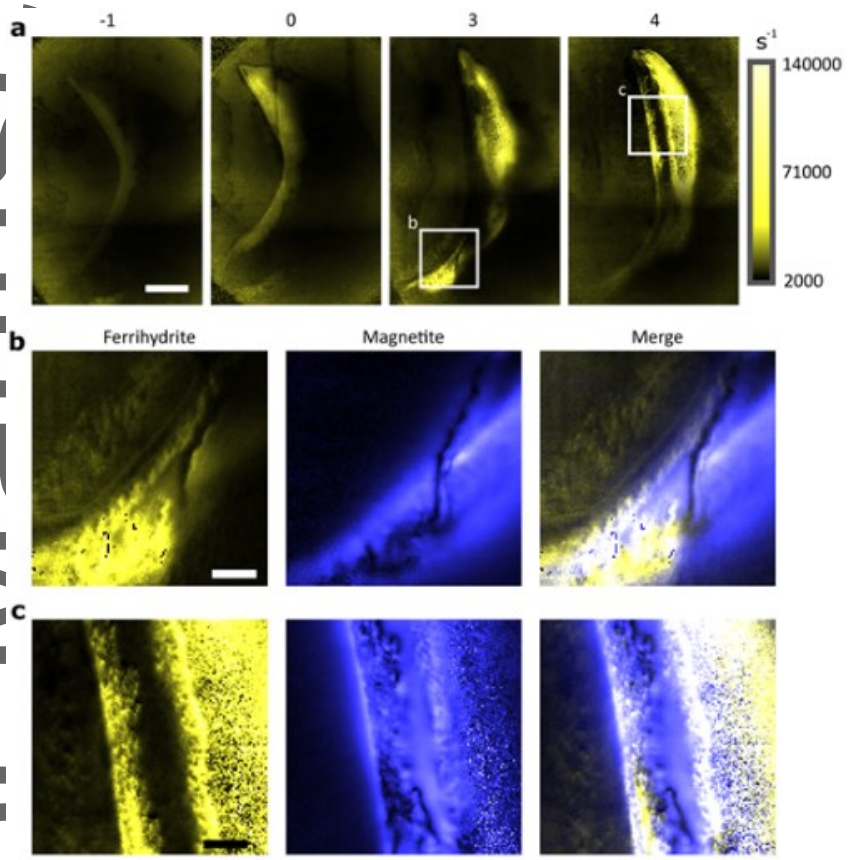


Figure 4. Superparamagnetic microscopy of chiton teeth. a, Quantum relaxometry images (1/T1) of the NV center in diamond showing the regions of superparamagnetic ferrihydrite. As the tooth develops, the total concentration and spatial distribution of ferrihydrite increases. Scale bar: 40 µm. b and c, show high resolution magnetic maps of ferrihydrite (1/T1) - yellow and magnetite (ODMR) - blue in various sections of the tooth. Areas of co-localization (white) reveal regions undergoing magnetic phase transformation. Scale bar: 10 µm

Author Manuscript

This article is protected by copyright. All rights reserved.

TOC

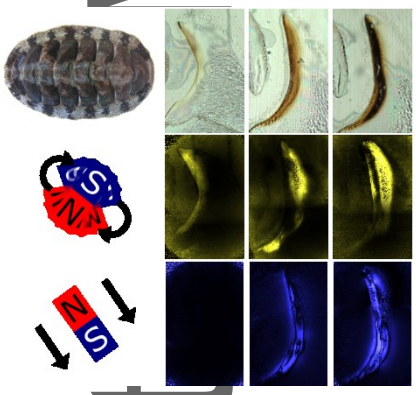
A quantum-based magnetic imaging technique for characterising iron biominerals is reported. Chitons - marine molluscs - are an ideal model of the poorly understood process of iron biomineralization. By applying diamond magnetic microscopy, the key components of chiton teeth, namely magnetite, and its precursor, ferrihydrite, are mapped with submicron resolution. Significantly, long-range magnetic order at early stages of tooth development is revealed.

Keyword: biomineralization, diamond, magnetic imaging, chiton, nitrogen-vacancy

Julia M. McCoey*, Mirai Matsuoka, Robert W. de Gille, Liam T. Hall, Jeremy A. Shaw, Jean-Philippe Tetienne, David Kisailus, Lloyd C. L. Hollenberg, and David A. Simpson*

Quantum Magnetic Imaging of Iron Biomineralization in Teeth of the Chiton *Acanthopleura hirtosa*

ToC figure



Author Manuscript

This article is protected by copyright. All rights reserved.